Image Reconstruction Under Contact Impedance Effect in Micro Electrical Impedance Tomography Sensors

Xiayi Liu, Jiafeng Yao, *Member, IEEE*, Tong Zhao, Hiromichi Obara, Yahui Cui, and Masahiro Takei, *Member, IEEE*

***Abstract*—Contact impedance has an important effect on micro electrical impedance tomography (EIT) sensors compared to conventional macro sensors. In the present work, a complex contact impedance effect ratio ξ is defined to quantitatively evaluate the effect of the contact impedance on the accuracy of the reconstructed images by micro EIT. Quality of the reconstructed image under various ξ is estimated by the phantom simulation to find the optimum algorithm. The generalized vector sampled pattern matching (GVSPM) method reveals the best image quality and the best tolerance to ξ. Moreover, the images of yeast cells sedimentary distribution in a multilayered microchannel are reconstructed by the GVSPM method under various mean magnitudes of contact impedance effect ratio $|\xi|$. The result shows that the best image quality that has the smallest voltage error $U_{\mathrm{E}} = 0.581$ is achieved with measurement frequency $f = 1$ MHz and mean magnitude $|\xi| = 26$. In addition, the reconstructed images of cells distribution become improper while $f < 10$ kHz and mean value of $|\xi| > 2400$.**

***Index Terms*—Contact impedance, electric double layer, micro electrical impedance tomography, multilayered microchannel.**

I. Introduction

Cell sensing is a key process for biochemical parameter characterization in biomedical applications. Guo demonstrated a very meaningful work: a pulse activated cell imaging system which greatly saves the memory needed during the imaging process [1], [2]. Tang developed a microfluidic impedance cytometer with inertial focusing and liquid electrodes for high-throughput cell counting and discrimination [3]. However, these methods could not detect the cells distribution in the cross-section of the microfluidic device. Current research points out the detection of cells' distribution in micro devices has the potential to improve the control of cells in microfluidic devices such as in the application of different cells separation. In this context, Electrical Impedance Tomography (EIT) has been widely used in application of biological industries since EIT reconstructs the distribution image based on the electrical properties of the cells with no radioactive source, non-invasiveness, fast measurement and low cost [4]. Since York developed a miniaturized electrical capacitance tomography sensor with an average sensor diameter of 750 μm comprising 8 to 16 electrodes [5], many researchers have been drawn attention to study the micro sensor for biological industries. Sun developed a miniaturized EIT sensor with a chip containing a circular 16-electrode array with diameter of 6 mm to visualize the cell culture process [6]. Yang applied a miniature EIT sensor to visualize 3D cell culture such as spheroids, artificial tissues and organs [7]. Chai used a Complementary Metal-Oxide- Semiconductor (CMOS) microchip with a planar array of electrodes to observe cellular behavior *in-vitro* [8]. With the development of micro manufacturing technology, size of EIT sensor is decreased from millimeter to micrometer order. In the previous study, our laboratory has developed a multi-layered microchannel which is integrated 80 platinum electrodes by MEMS technique and has a diamond shape with side length of 550 μm. The electrode-multi-layered microchannel has an advantage and potential to suit the cell sensing and manipulations [9]–[12].

In micro EIT sensing, a crucial problem is the effect of contact impedance on the interface between solution and electrodes. The contact impedance affects the measurements more seriously in micro EIT devices than conventional macro EIT sensors.

Many researchers are trying to improve the image quality with the consideration of the effect caused by contact impedance on the EIT sensing. Boyle and Adler show that a potential drop reaching to 53% in average contact impedance among electrodes affects seriously the quality of the reconstructed image [13]. Boverman proposed a new algorithm to improve the EIT image quality by compensating the poor contact of surface impedance [14]. Dardé and Stiboulis developed a complete electrode model to improve the measurement accuracy and image quality [15]. As their results, improving of image reconstruction algorithm

Manuscript received October 30, 2017; revised January 24, 2018 and March 14, 2018; accepted March 14, 2018. Date of publication May 15, 2018; date of current version June 5, 2018. This work was supported in part by Bio Assembler, Grant-in-Aid for Scientific Research on Innovative Areas of Japan, under Grant 26106708, in part by the National Natural Science Foundation of China under Grant 51706098 and Grant 51506175, and in part by the Natural Science Foundation of Jiangsu Province under Grant BK20170792. This paper was recommended by Associate Editor S. Sonkusale. *(Corresponding author: Jiafeng Yao.)*

X. Liu, T. Zhao, and Y. Cui are with the Faculty of Mechanical and Precision Instrument Engineering, Xi'an University of Technology, Xi'an 710048, China (e-mail: liu.xy@chiba-u.jp; tongzhao@xaut.edu.cn; cyhxut@xaut.edu.cn).

J. Yao is with the College of Mechanical & Electrical Engineering, Nanjing University of Aeronautics & Astronautics, Nanjing 210016, China (e-mail: jiaf.yao@nuaa.edu.cn).

H. Obara is with the Department of Mechanical Engineering, Tokyo Metropolitan University, Tokyo 192-0397, Japan (e-mail: obara@tmu.ac.jp).

M. Takei is with the Department of Mechanical Engineering, Chiba University, Chiba 263-0022, Japan (e-mail: masa2@chiba-u.jp).

Color versions of one or more of the figures in this paper are available online at http://ieeexplore.ieee.org.

Digital Object Identifier 10.1109/TBCAS.2018.2816946

and mathematic method become effective ways to reduce the effect of contact impedance in micro EIT sensing.

However, in micro EIT sensing, the principle of the contact impedance affecting the measurement is different from that of the macro one. Few researchers focus on the effect of contact impedance from the perspective of electro-chemical principle in micro device. Few researchers investigate the details of how contact impedance affects image quality and the key factor that affects contact impedance most in micro device. Furthermore, quantification of contact impedance effects on algorithms and the most suitable conditions for micro EIT become a crucial problem.

Algorithm of EIT image reconstruction is a key point of solving EIT inverse problem. The non-iterative and iterative algorithms were exhaustively reviewed by Yang and Peng [16]. Among the Conventional EIT algorithms applied to the micro EIT sensing, Tikhonov Regularization (TK) is a popular algorithm for solving linear equation systems or linear least-squares problems with a severely ill conditioned matrix, which replaces the given problem with a penalized least squares problem [17]. Projected Landweber Iteration (PLW) is widely used with the advantage of high image quality [18] because PLW improves the problem of time consumption during the iteration process. Generalized Vector Sampled Pattern Matching (GVSPM) is getting to be applied to solve the ill-posed inverse problem without empirical relaxation value to achieve stable convergence; mostly, GVSPM accomplishes high quality images in a few iterations [19].

The principle of micro EIT sensing is similar to the conventional macro EIT, which measures voltage under the condition of applied electrical current. Biophysical study reveals that the impedance measurements are frequency dependent [20]. At the relatively low-frequency, the cell/fluid solution is primarily affected by the electrical currents flowing around the cells (paracellular current) while at the relatively high frequency, the solution is primarily affected by the electrical currents flowing across the cell membranes (transcellular current) [21]. In the micro devices, the contact impedance in the range of frequency is also variable, it is decreased by frequency increases, but also depends on sensor size [22]. It is necessary to survey both contact impedance and cell solutions' impedance at various applied current frequencies because the contact impedance is also dependent on current frequency. In micro EIT sensing, the contact impedance is different from conventional macro sensing, which is the key point to the imaging accuracy of micro EIT; however, few researches work on it to clarify the tolerance of algorithms on contact impedance.

This paper focuses on the effect of contact impedance on the imaging quality of micro EIT. Firstly, a complex coefficient ξ which is called contact impedance effect ratio is defined to quantitatively evaluate the influence of contact impedance. Secondly, tolerability of the various image reconstruction algorithms to ξ is estimated by phantom simulation to determine the optimum algorithm for micro EIT. Finally, experiments of yeast cells sedimentation in a multi-layered microchannel are conducted to validate the effectiveness of the proper measurement condition and optimum algorithm of micro EIT.

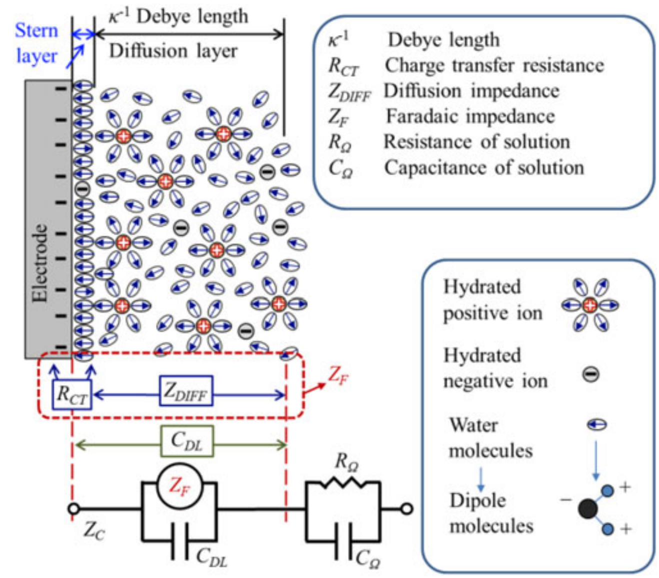

Fig. 1. Electrical properties on electrode surface and equivalent electrical circuit.

II. Principle Electro-Chemical Approach of Contact Impedance in Micro EIT Sensors

A. Principle Electro-Chemical Approach of Contact Impedance

Measurement results are affected by contact impedance in the interface of electrode and solution. In order to quantitatively evaluate the influence caused by contact impedance, a complex coefficient ξ which is called contact impedance effect ratio is defined as

$$\begin{aligned} \xi &= \xi_{\mathrm{Re}} + j\xi_{\mathrm{Im}} \\ \xi_{\mathrm{Re}} &= \frac{dR_C}{\kappa^{-1}R_\Omega}, \\ \xi_{\mathrm{Im}} &= \frac{dX_C}{\kappa^{-1}X_\Omega}, \\ |\xi| &= \sqrt{{\xi_{\mathrm{Re}}}^2 + {\xi_{\mathrm{Im}}}^2} \end{aligned} \quad (1)$$

where ξ_{Re} is the real part of ξ, ξ_{Im} is the imaginary part of ξ, $|\xi|$ is the magnitude value of ξ, R_C $[\Omega]$ is the real part of contact impedance Z_C $[\Omega]$, X_C $[\Omega]$ is the imaginary part of Z_C. R_Ω $[\Omega]$ is the real part of solution's impedance Z_Ω $[\Omega]$, X_Ω $[\Omega]$ is the imaginary part of Z_Ω. The equivalent circuit of contact impedance is shown in the bottom of Fig. 1. The result of ξ depends on the ratio of solution's impedance Z_Ω to contact impedance Z_C.

For the physical phenomenon of contact impedance shown in Fig. 1, once electrical current is injected to the electrode, contact impedance Z_C occurs in the electrical double layer (EDL) which includes the stern layer and diffusion layer. EDL is formed as ions and other charged species from the solution stick on the electrode surface in stern layer and diffuse in the diffusion layer. Under an assumption of the equivalent electrical circuit, Z_C is represented by a paralleled combination of capacitance of EDL C_{DL} [F/ m^2] and Faraday impedance Z_F [Ω] [22].

The EDL capacitance C_{DL} appears at the interface between the conductive electrode and solution. At this surface two layers of ions with opposing polarity form with an applied voltage are separated by ions adheres to the surface of the electrode and acts like a dielectric in a conventional capacitor. C_{DL} is expressed by [22]

$$C_{DL} = A\varepsilon_0\varepsilon_r/\kappa^{-1} \tag{2}$$

where κ^{-1} [m] is the Debye length, ε_0 [F/ m] is the vacum permitivitty $\varepsilon_0 = 8.854 \times 10^{-12}$ F/ m, ε_r is the relative permitivitty. Debye length κ^{-1} [22] is approximately calculated by

$$\kappa^{-1} = \sqrt{\frac{\varepsilon_0\varepsilon_r k_B T}{2n_e {n_z}^2 e^2}} \tag{3}$$

where k_B [J/ K] is the Boltzmann constant $k_B = 1.38 \times 10^{-23}$ J/ K, e [C] is the elementary charge $e = 1.60 \times 10^{-19}$ C, and n_e [m^{-3}] is the ion density.

The contact impedance Z_C [Ω] is expressed by

$$Z_C = 1/\left(1/Z_F + j\omega C_{DL}\right) \tag{4}$$

Z_F is represented by a series combination of charge transfer resistance R_{CT} [Ω] and diffusion impedance Z_{DIFF} [Ω] [22]. Z_{DIFF} occurs by the migration and convection of ions in the diffusion layer. Here, Z_{DIFF} is treated as semi-infinite diffusion at the frequency range from $f = 10$ Hz to $f = 5$ MHz. R_{CT} occurs when the interface which is perturbed by the charges in the both side of interface take place. Z_F is expressed by

$$Z_F = R_{CT} + Z_{DIFF} = \frac{R_G T}{n_z F i_0} + \frac{R_G T}{{n_z}^2 F^2 c_0 A (2\pi f D j)^{1/2}} \tag{5}$$

where R_G is the gas constant $R_G = 8.31$ J/ (K mol), T [K] is the absolute temperature, n_z is the integer charge number, F is the Fraday constant $F = 96500$ C/ mol, i_0 [A] is the electrode current, A [m^2] is the area surface of the electrode, f [Hz] is frequency of exciting alternating current (AC), c_0 [mol/m^3] is the charge concentration and D [m^2/s] is the ions diffusion coefficient, they are depended on the positive/negative ions.

Moreover, R_Ω [Ω] and X_Ω [Ω] in Eq. (1) represent the real part and the imaginary part of solution impedance Z_Ω [Ω], respectively, which are expressed as:

$$\begin{aligned} Z_\Omega &= R_\Omega + jX_\Omega \\ R_\Omega &= \frac{Ad\sigma_c}{A^2{\sigma_c}^2 + 4\pi^2 f^2 {\varepsilon_0}^2 {\varepsilon_{rc}}^2 A^2} \\ X_\Omega &= \frac{2\pi f d\varepsilon_0\varepsilon_{rc} A}{A^2{\sigma_c}^2 + 4\pi^2 f^2 {\varepsilon_0}^2 {\varepsilon_{rc}}^2 A^2} \end{aligned} \tag{6}$$

where d [m] is the distance between electrodes, A [m^2] is the surface of electrode, σ_c is the conductivity of cells solution.

According to the definition of contact impedance effect ratio ξ, the value of ξ is frequency depended. Fig. 2 shows the real part ξ_{Re}, the imaginary part ξ_{Im} and the magnitude $|\xi|$ of cells solution at different frequencies. The results are calculated from (1) based on the value of the parameters shown in Table I. As shown in Fig. 2, the frequency affects ξ seriously. In the low frequencies

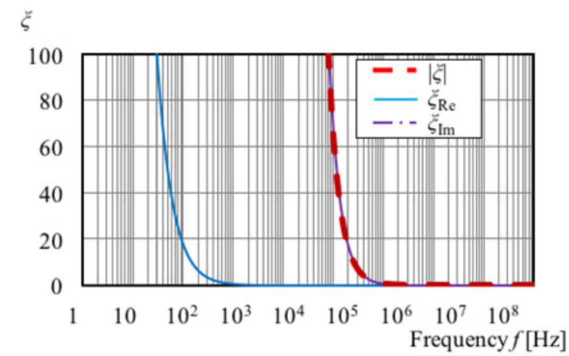

Fig. 2. Effect of contact impedance by frequency in micro EIT sensor.

TABLE I
SYMBOL AND VALUES OF CALCULATION IN ξ AND THE COMPARISON OF MACRO AND MICRO SENSORS

Symbol	Quantity
R_G	Gas constant [J·K^{-1}·mol^{-1}]
T	Absolute temperature [K]
n_z	Valence charge number
F	Fraday constant [C/mol]
i_0	Exchange current [A]
c_0	Charge concentration [mol/m^3]
A	Electrode surface [m^2]
d	Distance of electrode pair
D	Ions diffusion coefficient [m^2/s]
κ^{-1}	Debye length [m]
ε_0	Permitivitty of vacuum [F/m]
ε_{rw}	Reletive permitivitty of pure water [-]
ε_{rc}	Reletive permitivitty of cells solution [-]
σ_w	Conductivity of pure water [S/m]
σ_c	Conductivity of cells solution [S/m]

at $f < 100$ kHz, the value of ξ_{Im} and $|\xi|$ are much larger than the frequency in the case of $f > 100$ kHz. The real part has the same tendency, in the low frequencies at $f < 100$ Hz, the value of ξ_{Re} is much larger than the frequency in the case of $f > 100$ Hz. It reveals that contact impedance affects the measurements more strongly. The value of ξ_{Re} and ξ_{Im} are converged to a very small value at $f = 1$ kHz and $f = 1$ MHz respectively. The magnitude $|\xi|$ almost coincides with the ξ_{Im}. This phenomenon means that imaginary part of contact impedance impacts the measurement greatly.

In addition, from the principle of electrical chemical contact impedance, ξ led to different impact on the measurements of micro EIT sensors and conventional macro EIT sensors. Mostly, the obvious difference of micro and macro EIT sensors is the surface area. Fig. 3 shows the comparison of real part, imaginary part and magnitude of Z_C for micro and macro EIT sensor calculated by (2) in a frequency range from $f = 1$ Hz to $f = 100$ MHz. Surface area of micro and macro EIT sensor is assumed as $A_{\mathrm{micro}} = 2 \times 10^{-9}$ m^2 (200 μm × 10 μm) and $A_{\mathrm{macro}} = 2 \times 10^{-5}$ m^2 (4 mm × 10 mm) respectively. Table I shows the summarized other relevant parameters used in the calculation. As shown in Fig. 2, the magnitude of Z_C for macro sensor is decreased rapidly in the frequency range $f < 100$ Hz, but for micro EIT sensors, it decreased rapidly in the frequency range $f < 100$ kHz. The comparison shows the frequency range

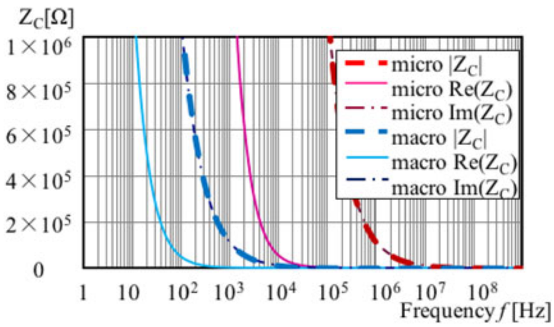

Fig. 3. Comparison of impedance in micro EIT sensor and macro sensor by calculation.

affected by contact impedance in micro EIT sensors is much larger than macro sensor. The real part and imaginary part of contact impedance have same consequences with the magnitude. This phenomenon is induced by the different electrode surface area between micro EIT sensor and conventional macro sensor. This phenomenon causes the frequency range affected by contact impedance in micro EIT sensors is much larger than macro sensors. Therefore, micro EIT sensors are much more insensitive than macro sensors at low frequencies because of the large contact impedance.

III. Simulation of Algorithms Affected by Contact Impedance

A. Simulation Methods

In order to find the optimum image reconstruction algorithm for micro EIT, qualities of the reconstructed images obtained by different image reconstruction algorithm are quantitatively estimated under various contact impedance effect ratio ξ. The widely-used algorithms, GVSPM (Generalized Vector Sampled Pattern Matching), TK (Iterative Tikhonov Regularization) and PLW (Projected Landweber Iteration), are employed in the present study.

The governing equation of GVSPM [19] is:

$$\sigma^{(k)} = \sigma^{(k-1)} - J^T \left(\frac{J\sigma^{(k)}}{\left| J\sigma^{(k)} \right|} - U'_T \right) \tag{7}$$

where J is the sensitive matrix, and U'_T is the normalized potential matrix from experiment and $\sigma^{(\boldsymbol{k})}$ is the kth iteration normalized conductivity. The first iterative conductivity value $\sigma^{(0)}$ is obtained from the LBP (Linear Back Projection) method expressed by

$$\sigma^{(0)} = J^T U_T / J^T I \tag{8}$$

where I is the unit matrix, U_T is the measured voltage.

The equation of TK [17] is expressed by

$$\sigma^{(0)} = \left(J^T J + \mu I \right)^{-1} J^T - U_T \tag{9}$$

$$\sigma^{(k+1)} = \sigma^{(k)} + \left(J^T \cdot J + \mu I \right)^{-1} \left(J^T \cdot U_T + \mu \sigma^{(k)} \right) \tag{10}$$

where μ is the empirical coefficient as a small positive number, I is an unit matrix, the first iterative conductivity value $\sigma^{(0)}$ is obtained by (9).

TABLE II
List of Measurements

Measurement no.	Electrode transmitters		Electrode receivers	
	H_C	L_C	H_P	L_P
1	1	9	2	8
2	1	9	3	8
3	1	9	4	8
4	1	9	5	8
5	1	9	6	8
6	1	9	7	8
7	1	9	10	8
8	1	9	11	8
9	1	9	12	8
10	1	9	13	8
11	1	9	14	8
12	1	9	15	8
13	1	9	16	8
...	...	...	...	...
14	2	10	3	9
15	2	10	4	9
...	...	...	...	...
27	3	11	4	10
...	...	...	...	...
104	8	16	7	15

PLW is the most widely used iterative method for EIT to reconstruct images [18]. The solution is expressed by

$$f(\sigma) = \sigma^{(k+1)} = P\left[\sigma^{(k)} + \mu J^T \left(U_T - J \cdot \sigma^{(k)} \right) \right] \tag{11}$$

where P is a projection operator defined by

$$P[f(\sigma)] = \begin{cases} 0 & \text{if} \quad f(\sigma) < 0 \\ f(\sigma) & \text{if} \quad 0 < f(\sigma) < 1 \\ 1 & \text{if} \quad f(\sigma) > 1 \end{cases} \tag{12}$$

the first iterative conductivity value $\sigma^{(0)}$ is obtained from the LBP method as shown in (8), U_{T} is the measured voltage.

In the simulation, ξ is employed as an impact factor to the input voltage data. It is described as (13), which affects the value of input voltage. In the simulation, all the input voltage is calculated at a range of ξ.

$$u_i = u_{\Omega i} \left(1 + \xi \kappa^{-1} / d_i \right) \tag{13}$$

where i is the ith measurement number while, Table II shows the measurements strategy of different electrode pairs, the samples of H and L are high potential and low potential. The total number is $M = 104$. u_i is the ith-measured voltage, $u_{\Omega i}$ is the solution voltage of ith measurement, d_i is the distance of ith-measured electrode pair.

Image error I_E is a common coefficient to evaluate image quality in phantom simulation [19], which is calculated as:

$$I_E = \frac{\sqrt{\sum_{j=1}^{N} \left(\sigma_j^{(K)} - \sigma_j^{(ori)} \right)^2}}{\sqrt{\sum_{j=1}^{N} \left(\sigma^{(ori)} \right)^2}} \tag{14}$$

where $\sigma_i^{(K)}$ is the jth element and Kth iteration of the reconstructed image, K is the final iteration of the calculation. σ_j^{ori} is the jth element of the original image conductivity. N is the pixel number of the image. The lower value of I_E indicates a better image quality.

Another coefficients ψ_{IE} is defined to evaluate the variation of I_E in a range of ξ, which is explained as:

$$\psi_{IE} = \frac{I_E^{(\max)} - I_E^{(\min)}}{I_E^{(\min)}} \times 100\% \tag{15}$$

where $I_E^{(\max)}$ is the maximum of I_E, $I_E^{(min)}$ is the minimum of I_E, the lower value ψ_{IE} indicates a smaller variation.

B. Simulation Conditions

In the simulation, two phantoms are created. The first phantom is created as 10 vol% cells solution which deposited at the bottom of domain. The second phantom is created as a cells group in the center of the domain. In the phantoms, the water conductivity is $\sigma_{\mathrm{w}} = 5.5 \times 10^{-6}$ S/ m, and the cells conductivity is $\sigma_{\mathrm{c}} = 2.34 \times 10^{-3}$ S/ m. In the simulation, 16 electrodes were equally spaced at the periphery of the multi-layered microchannel. Considering that the tendencies of $|\xi|$ and ξ_{Re} are same, DC current is applied to simplify the condition. Therefore, the imaginary part of ξ is ignored as $|\xi| = \xi_{\mathrm{Re}}$. The current $i_C = 0.1$ mA was injected through opposite electrode pairs while the voltage responses across the remaining pairs were recorded in accordance with the order shown in Table II. For each current injection, the voltages were obtained by solving Poisson equation using finite-element method. The range of $|\xi|$ is varied from $|\xi| = 0$ to $|\xi| = 100$. Resolution of reconstructed image is $N = 32 \times 32 = 1024$. The optimum empirical coefficient μ in PLW and TK are chosen in a range of value by comparing I_E.

C. Simulation Results

Fig. 4(a) shows the simulation results of the relative conductivity distribution which is reconstructed by different algorithms and $|\xi|$. As shown in Fig. 4(b) and (c), image errors I_E of the three algorithms in both phantoms are increased as $|\xi|$ increases. It means the larger $|\xi|$ affects image quality more. From the chart of Fig. 4(b), in the case of $|\xi| = 0$, I_E value of GVSPM ($I_E = 0.572$) is smaller than I_E value of TK ($I_E = 0.587$) and PLW ($I_E = 0.586$). In the case of $|\xi| = 100$, I_E value of GVSPM ($I_E = 0.583$) is smaller than I_E value of TK ($I_E = 0.607$) and PLW ($I_E = 0.618$). From the chart of Fig. 4(c), in the case of $|\xi| = 0$, I_E value of GVSPM ($I_E = 0.721$) is smaller than I_E value of TK ($I_E = 0.828$) and PLW ($I_E = 0.739$). In the case of $|\xi| = 100$, I_E value of GVSPM ($I_E = 0.792$) is smaller than I_E value of TK ($I_E = 0.911$) and PLW ($I_E = 0.815$). GVSPM achieves better image quality than other two because it presents the smallest image error in each value of $|\xi|$. The reason is that GVSPM have no empirical coefficient like μ in PLW and TK. The variation of I_E in phantom 1 by GVSPM in the range of $|\xi|$ is $\psi_{IE} = 1.99\%$, smaller than PLW which is $\psi_{IE} = 5.33\%$ and TK which is $\psi_{IE} = 3.54\%$. The results in phantom 2 of GVSPM is $\psi_{IE} = 9.81\%$, which are smaller than PLW of $\psi_{IE} = 10.23\%$ and TK of $\psi_{IE} = 9.94\%$. These results reveal that GVSPM has a better toleration of ξ.

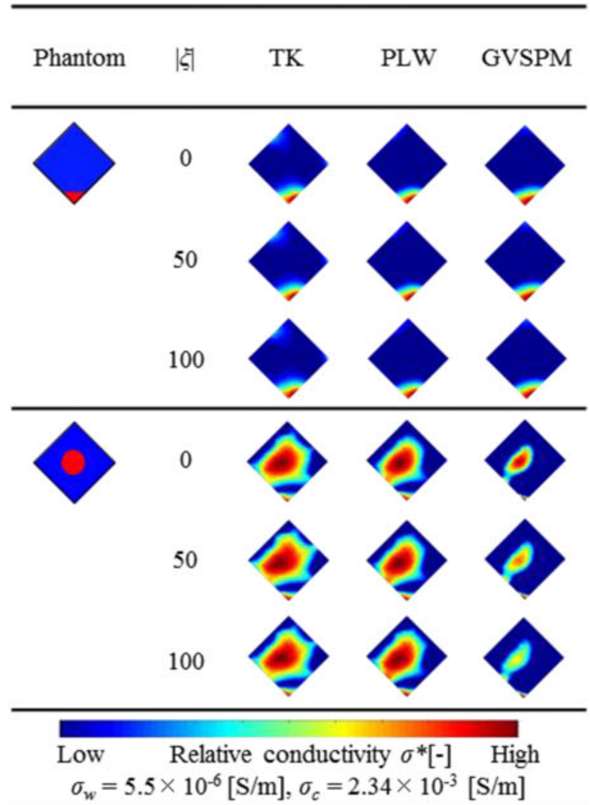

(a)

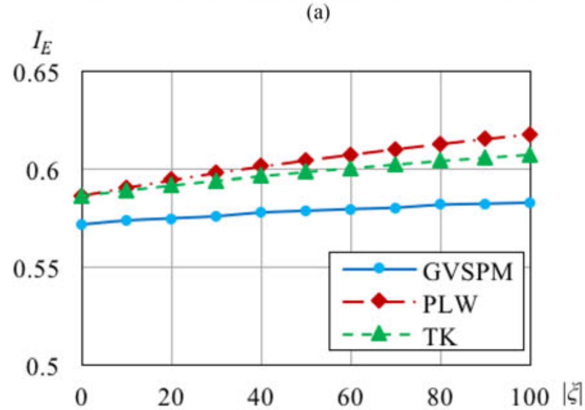

(b)

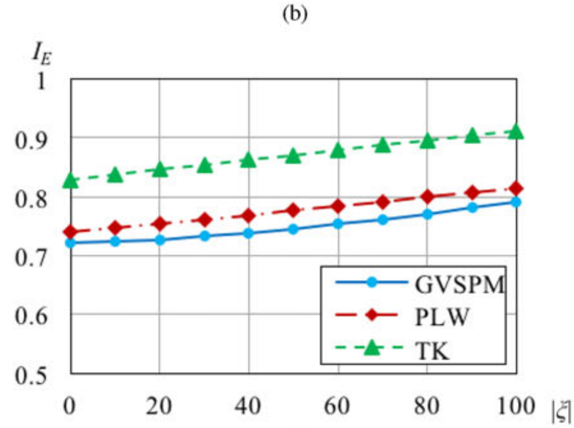

(c)

Fig. 4. Simulation results. (a) Image reconstructed by different algorithms, (b) I_E of 1st Phantom in different $|\xi|$, and (c) I_E of 2nd Phantom in different $|\xi|$.

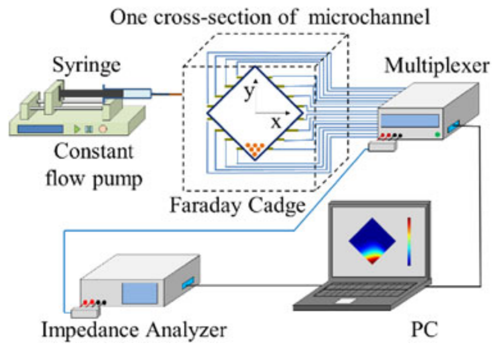

Fig. 5. Experimental set-up.

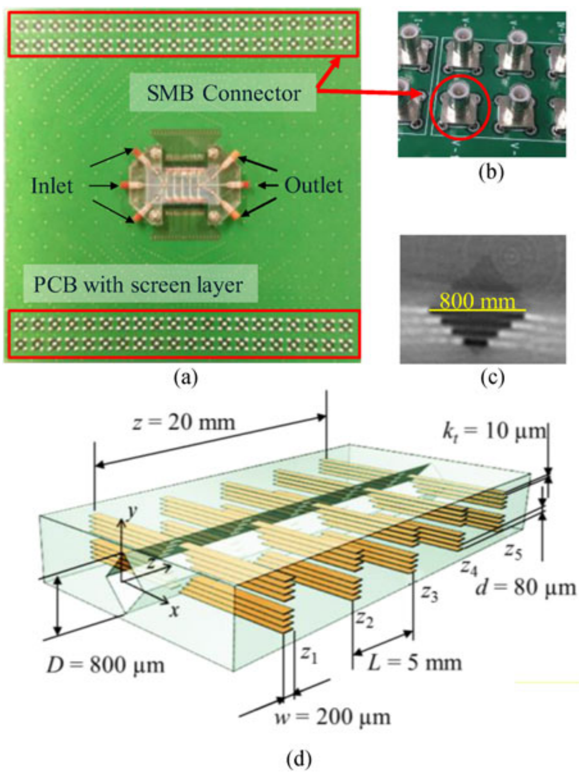

Fig. 6. Multi-layered microchannel. (a) Photograph of the microchannel and connectors, (b) SMB connectors, (c) microcomputed tomography image, and (d) dimension of the microchannel.

IV. Experiments of Micro EIT Images Quality in ξ

A. Experimental Setup

As shown in Fig. 5, the experimental setup is consisted of a multi-layered microchannel, a syringe pump (Muromachi KDS-100), a Faraday cage, a multiplexer (Agilent 34970A, matrix switch Model Agilent 34904A), an impedance analyser (HIOKI IM3570) and a PC (Mouse computer W950JU). Fig. 6(a) shows the details of multi-layered microchannel. It is fixed on a PCB (printed circuit board). The connectors are SMB (Sub Miniature Version B) as shown in Fig. 6(b). Fig. 6(c) shows the micro CT (computed tomography) image of one cross-section in the multi-layered microchannel, which is obtained by the X-Ray CT scanner (Model: TDM1300-IS, Yamato Scientific, Japan). The dimension of the multi-layered microchannel is shown in Fig. 6(d). The length of the main flow channel is $z = 20\,\text{mm}$. Five electrode-integrated cross-sections with separation distance $L = 5\,\text{mm}$ are arrayed along the main flow-channel. The diagonal of the diamond cross-section is $D = 800\,\mu\text{m}$. In each section, 16 platinum electrodes are integrated. The thickness of electrode is $k_t = 10\,\mu\text{m}$ and the width is $w = 200\,\mu\text{m}$, the distance between two adjacent electrodes is $d = 80\,\mu\text{m}$.

B. Experimental Methods

Experiments are conducted to visualize the cells distribution by EIT method with different values of magnitude $|\xi|$. GVSPM was employed to reconstruct the image due to its best image quality and tolerance of ξ shown in the simulation. Contact impedance Z_C and impedance of cells solution Z_Ω are calculated by fitting the experimental results of EIS (Electrical Impedance Spectroscopy) in each measured electrode pair. The equivalent circuit is shown in Fig. 1. $|\xi|$ is calculated by (1) from the value of fitted Z_C and Z_Ω in each electrode pair. In the measurements, the measured impedance Z is

$$Z = Z_C + Z_\Omega \tag{16}$$

as Z_C and Z_Ω are in series. After the calculation, the values of $|\xi|$ in the supported frequency are selected to evaluate the effect of contact impedance.

In the reconstruction of an EIT image, all the voltages from different electrode pairs are measured at a fixed frequency. The number of $|\xi|$ is the same as the number of measurements M which is shown in Table II, the mean value of $|\xi|$ is calculated to evaluate the effect of contact impedance in the frequency.

The voltage error U_E is employed to evaluate the image quality,

$$U_E = \frac{\sqrt{\sum_{i=1}^{M}\left(u_i^{(K)} - u_i^{(\exp)}\right)^2}}{\sqrt{\sum_{i=1}^{M}\left(u_i^{(\exp)}\right)^2}} \tag{17}$$

where i is the ith measurement number, the measurement strategy is as Table II. M is the total number of measurements. $u_i^{(K)}$ is the ith element of the final iterative potential which is calculated from the final $k = K$ iterative reconstructed image, u_i^{exp} is the ith measured voltage from experiments. U_E quantifies the difference between $u_i^{(k)}$ and $u_i^{(exp)}$. A smaller value of U_E means better image quality.

C. Experiential Conditions

The measurement object of the experiments is yeast cells sedimentary distribution. The temperature of culturing yeast cells is $T = 298\,\text{K}$. The volume concentration of cell solution is $\Phi = 10\,\text{vol\%}$ which is mixed by yeast cells and pure water. The flow rate of the injected solution to the multi-layered microchannel by the syringe pump is $Q = 10\,\text{mL/ h}$. The cells deposition time is 30 min, after that, the measurement starts. The applied alternate current is $i_C = 0.1\,\text{mA}$. The frequencies for image reconstruction are $f = 10\,\text{kHz}, 50\,\text{kHz}, 100\,\text{kHz}, 500\,\text{kHz}$ and $1\,\text{MHz}$. The number of measured electrode pairs at each frequency is $M = 104$. The resolution of the reconstructed image is $N = 32 \times 32 = 1024$.

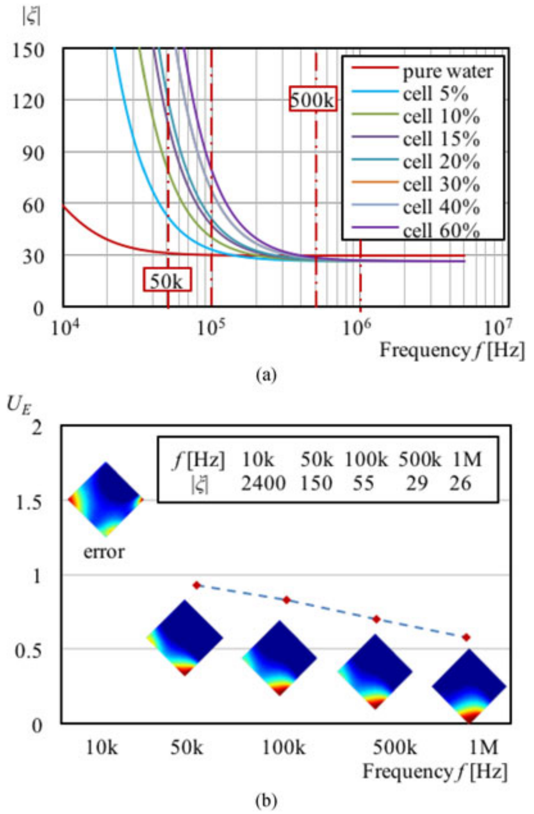

Fig. 7. Experiment results. (a) $|\xi|$ by frequency on different concentration solutions and (b) reconstructed EIT images.

D. Experimental Results

As the different distance of electrode pairs around the microchannel, the concentrations of cells in different electrode pairs are different while cells at the bottom of the multi-layerd microchannel. Fig. 7(a) shows the magnitude values $|\xi|$ in different concentration of yeast cell solutions by a range of frequencies. At $f = 10\,\text{kHz}$, $|\xi|$ under cell concentration $\Phi = 0$ to 60% is increased from $|\xi| = 70$ to $|\xi| = 4500$; at $f = 1\,\text{MHz}$, this value increased from $|\xi| = 26$ to $|\xi| = 27$. The results show the variation of $|\xi|$ influenced by different cells concentration is much smaller than different frequency. In addition, the variation of $|\xi|$ is much smaller than the condition of $f >$ 100 kHz. In the frequency range of $f <$100 kHz, the contact impedance affects the measurement seriously. In the case of $f >$ 100 kHz, the effect is much smaller. The image quality of different ξ is affected by the different frequencies. From the results, the effect of contact impedance is predicted.

Fig. 7(b) shows the reconstructed images at different mean values of $|\xi|$. At lower frequencies $f = 10\,\text{kHz}$, the mean values of $|\xi|$ is very large as $|\xi| = 2400$, the reconstructed image displays an incorrect cell distribution, since the correct one shows the distribution of cells at the bottom of the multi-layered microchannel due to sedimentation. In the case of higher frequencies as $f >$ 50 kHz, the mean value of $|\xi|$ are decreased from $|\xi| = 150$ to $|\xi| = 26$. From the comparison, the smallest $U_E = 0.581$ is found out at the smallest mean value $|\xi| = 26$ at $f = 1\,\text{MHz}$.

From the result, contact impedance affects the image quality significantly. The much larger value of $|\xi|$ affects measurement seriously and prevents correct reconstructed images. The small value of $|\xi|$ affects measurement less, the EIT images are correct and have a better image quality.

V. Discussion

As addressed above, both the simulation and experiment results reveal serious negative effects of the contact impedance on micro EIT. However, these effects are also shown to be reducible by using a suitable algorithm and optimum frequency. Particularly, GVSPM shows better image reconstruction quality and toleration of contact impedance than PLW and TK. There are two reasons for the superiority of GVSPM.

Firstly, according to the governing equation of PLW, TK and GVSPM, PLW and TK method need empirical coefficient μ for each iteration process, which is important for solving the inverse problem. In PLW, μ is the relaxation factor, which controls the convergence for each iteration process. In TK, μ is regularization parameter, which regulars the results and improves the accuracy for each iteration process. However, the GVSPM method does not need an empirical value. It uses an inner product as the objective function of convergence in the iterative solution which is an advantage of self-convergence [19]. With this advantage, GVSPM has a better convergence controlling performance. PLW and TK are converged by the supported critical value, and they have no feasibility of self-convergence.

Secondly, GVSPM is less sensitive to contact impedance effect than PLW and TK. A coefficient I_P (inner product) is employed to discuss the convergence of algorithms in a range of $|\xi|$. In this method, the input voltage is treated as a unit vector expressed as $U^{(inp)}/|U^{(inp)}|$, and the calculated voltage from conductivity is also treated as a unit vector expressed as $J\sigma^{(k)}/|J\sigma^{(k)}|$. The inner product of the two vectors is closer to 1 since they are similar which means the reconstructed image is closed to the true cells distribution. An inner product value closes to 1 is a sufficient condition to measure cell distribution accurately.

In this paper, I_P is expressed by

$$I_P = \frac{U^{(\text{inp})}}{\left|U^{(\text{inp})}\right|} \cdot \frac{J\sigma^{(k)}}{\left|J\sigma^{(k)}\right|} \tag{18}$$

where $U^{(inp)}$ is the input voltage, J is the sensitive matrix, $\sigma^{(k)}$ is the calculated conductivity in kth iteration. The value of I_P is closer to 1 means the image quality is better. Another coefficients ψ_{IP} is defined to evaluate the variation of I_P in a range of ξ, which is explained as:

$$\psi_{IP} = \frac{I_P^{(\max)} - I_P^{(\min)}}{I_P^{(\max)}} \times 100\% \tag{19}$$

where $I_P^{(\max)}$ is the maximum of I_P, $I_P^{(\min)}$ is the minimum of I_P, the lower value ψ_{IP} indicates a smaller variation.

Fig. 8 shows the results of first phantom in Fig. 4(a), from the result, I_P is decreased while $|\xi|$ increases. GVSPM has a better image quality as the inner product decreased from 0.756 to 0.726 while the value of $|\xi|$ from $|\xi| = 0$ to $|\xi| = 100$, the results of TK are from 0.733 to 0.701 and PLW are from 0.745 to 0.717. In addition, the variation of I_E by GVSPM in the range of $|\xi|$

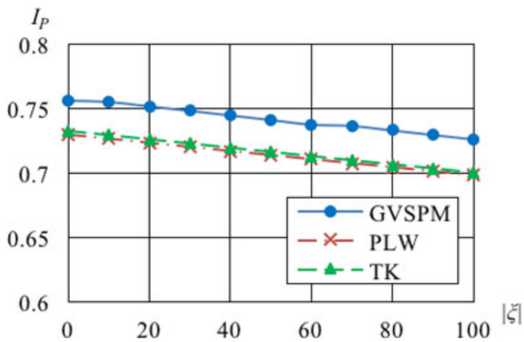

Fig. 8. Comparison of inner product in different $|\xi|$.

is $\psi_{IE} = 1.99\%$, smaller than PLW which is $\psi_{IE} = 5.33\%$ and TK which is $\psi_{IE} = 3.54\%$. The smallest variation of the inner product is $\psi_{IP} = 3.96\%$ by GVSPM, the result of TK is $\psi_{IP} = 4.45\%$ and PLW is $\psi_{IP} = 4.31\%$. As a result, GVSPM is better than other algorithms to tolerate the effect at the range of $|\xi|$. The reason lies in the fact that contact impedance effects are reduced by the division of unit vectors normalization in GVSPM. From (10) and (11), TK and PLW have no function to reduce $|\xi|$ in the iteration. Both are regulated by the empirical coefficients which are constant value and have a linear relationship with $|\xi|$.

Equation (13) shows the composing of measured voltage, it is also expressed by

$$u_i = u_{\Omega i} + u_{\Omega i} \left(\xi \kappa^{-1} / d_i\right) \tag{20}$$

the first term ($\xi = 0$) is constant. The key point is GVSPM has the characteristics to reduce the right second term. In (7), it is clear the regular part $J\sigma^{(k)} / |J\sigma^{(k)}|$ has a division, both numerator and denominator have the component of $|\xi|$. In the division, the effect of $|\xi|$ is reduced.

In the experiments, contact impedance affects the image quality in different conditions. At the lower frequencies $f <$ 100 kHz, the measured voltages are mainly from the potential drop of the contact impedance. In the case of frequency $f = 10$ kHz, the mean value of $|\xi|$ is $|\xi| = 2400$, from (13), the mean ratio of the contact impedance potential drop in measured voltage is 87%, which reveals that, the voltages used for reconstructing the images are not from cells solution but mainly from contact impedance. Hence the images are not able to display the real cell distribution. At the frequencies 100 kHz $< f <$ 1MHz, the contact impedance ratio ξ is reduced to a very small range as $26 < |\xi| < 55$. In this condition, the mean ratio of the contact impedance potential drop in measured voltage is from 7% to 20%, it means the contact impedance accounts for a small proportion of the measured voltage. Hence the reconstructed images display the cell distribution well at higher frequencies. Boone and Holder indicated that 20% variation of contact impedance results in an image that is enough to render the image in the previous study [23].

In addition, the contact impedance effect ratio ξ clarifies and quantizes the influence of contact impedance in micro EIT sensors, and explains the optimum frequency for micro EIT sensing. It is summarized by the principle of contact impedance of electrode-solution. For further research, the principle is feasible to be applied in the situation which has the contact impedance in the interface such as EDL (electrical double layer).

VI. Conclusion

In this paper, a contact impedance effect ratio ξ was defined to evaluate quantitatively the effect of contact impedance on micro EIT image quality. Based on ξ, simulation and experiments were conducted.

1) Contact impedance effect ratio ξ was defined to clarify the effect of contact impedance. The value of ξ was calculated by fitting the experimental data. In the micro EIT sensor, the measuring frequency affects the value of ξ much more than concentrations. From the result, the measurement data in the frequency range of $f <$ 100 kHz is seriously affected by contact impedance, and the frequency range of $f >$ 100 kHz is suitable for EIT measurement.
2) In the simulation, three different image reconstruction algorithms (GVSPM, TK and PLW) were compared by a range of ξ. GVSPM is the optimum algorithm due to its best image quality and smallest variation $\psi = 1.99\%$ in the range from $\xi = 0$ to $\xi = 100$.
3) In the experiments, the images of cell sedimentation at the bottom of multi-layered microchannel from different mean value of $|\xi|$ are reconstructed by GVSPM. The results proved the inference that smaller value of $|\xi|$ affects the image quality slightly and higher value of $|\xi|$ affects the image quality seriously. In the case of the mean value of $|\xi| < 150$ at the frequency range of $f >$ 50 kHz, the images are correct and the image quality is high, the best image quality $U_E = 0.581$ is achieved at the smallest value as $|\xi| = 26$. In the case that the mean value of $|\xi|$ is very large at low frequencies $f <$10 kHz, the images are not able to display the real cell distribution.

References

[1] J. Guo, X. Huang, and Y. Ai, “On-demand lensless single cell imaging activated by differential resistive pulse sensing,” *Anal. Chem.*, vol. 87, no. 13, pp. 6516–6519, 2015.

[2] J. Guo *et al.*, “Portable resistive pulse-activated lens-free cell imaging system,” *RSC Adv.*, vol. 4, no. 99, pp. 56342–56345, 2014

[3] W. Tang *et al.*, “Microfluidic impedance cytometer with inertial focusing and liquid electrodes for high-throughput cell counting and discrimination,” *Anal. Chem.*, vol. 89, no. 5, pp. 3154–3161, 2017.

[4] R. Bayford and A. Tizzard, “Bioimpedance imaging: an overview of potential clinical applications,” *Analyst*, vol. 137, no. 20, pp. 4635–4643, 2012.

[5] T. A. York *et al.*, “A miniature electrical capacitance tomography,” *Meas. Sci. Technol.*, vol. 17, no. 8, pp. 2119–2129, 2006.

[6] T. Sun *et al.*, “On-chip electrical impedance tomography for imaging biological cells,” *Biosensors Bioelectron.*, vol. 25, no. 5, pp. 1109–1115, 2010.

[7] Y. Yang *et al.*, “A miniature electrical impedance tomography sensor and 3D image reconstruction for cell imaging,” *IEEE Sensors J.*, vol. 17, no. 2, pp. 514–523, Jan. 2017.

[8] K. T. C. Chai, J. H. Davies and D. R. S. Cumming, “Electrical impedance tomography for sensing with integrated microelectrodes on a CMOS microchip,” *Sensors Actuators B: Chem.*, vol. 127, no. 1, pp. 97–101, 2007.

[9] J. Yao *et al.*, “Development of three-dimensional integrated multi-layered microchannel-electrode system to understand the particles’ movement with electrokinetics,” *Biomicrofluidics*, vol. 10, no. 2, 2016, Art. no. 024105.

[10] T. Zhao *et al.*, "Investigation of particle inertial migration in high particle concentration suspension flow by multi-electrodes sensing and Eulerian-Lagrangian simulation in a square microchannel," *Biomicrofluidics*, vol. 10, no. 2, 2016, Art. no. 204120.

[11] J. Yao and M. Takei, "Application of process tomography to multiphase flow measurement in industrial and biomedical fields—A review," *IEEE Sens. J.*, vol. 17, no. 24, pp. 8196–8205, Dec. 2017.

[12] J. Yao *et al.*, "Distinct motion of GFP-tagged histone expressing cells under AC electrokinetics in electrode-multilayered microfluidic device," *IEEE Trans. Biomed. Circuits Syst.*, vol. 11, no. 6, pp. 1450–1458, Dec. 2017.

[13] A. Boyle and A. Adler, "Impact of electrode area, contact impedance and boundary shape on EIT images," *Physiol. Meas.*, vol. 32, no. 7, pp. 745–754, 2011.

[14] B. S. Kim *et al.*, "The complete electrode model for EIT in a mammography geometry," *Physiol. Meas.*, vol. 28, no. 7, pp. 1–17, 2007.

[15] D. Dardé and S. Stiboulis, "Electrode modelling: The effect of contact impedance," *ESAIM: Math. Model. Numer. Anal.*, vol. 50, no. 2, pp. 415–431, 2016.

[16] W. Yang and L. Peng, "Image reconstruction algorithms for electrical capacitance tomography," *Meas. Sci. Technol.*, vol. 14, no. 1, pp. R1–R13, 2002.

[17] M. Vauhkonen *et al.*, "Tikhonov regularization and prior information in electrical impedance tomography," *IEEE Trans. Med. Imag.*, vol. 17, no. 2, pp. 285–293, Apr. 1998.

[18] L. Peng, H. Merkus, and B. Scsarlett, "Using regularization methods for image reconstruction of electrical capacitance tomography," *Part. Part. Syst. Charact.*, vol. 17, no. 3, pp. 96–104, 2000.

[19] M. Takei and Y. Saito, "Application of the generalized vector sampled pattern matching method to reconstruction of electrical capacitance CT images," *Meas. Sci. Technol.*, vol. 15, no. 7, pp. 1371–1381, 2004.

[20] K. Asami *et al.*, "Dielectric spectroscopy of biological cells," *Bioelectrochemistry Bioenergetics*, vol. 40, no. 2, pp. 141–145, 1996.

[21] C. Xiao *et al.*, "An in-depth analysis of electric cell-substrate impedance sensing to study the attachment and spreading of mammalian cells," *Anal. Chem.*, vol. 74, no. 6, pp. 1333–1339, 2002.

[22] V. F. Lvovich, "Impedance representation of bulk-material and electrode processes," in *Impedance Spectroscopy*. New York, NY, USA: Wiley, 2012, pp. 71–85.

[23] K G Boone and D S Holder, "Effect of skin impedance on image quality and variability in electrical impedance tomography: a model study," *Med. Biol. Eng. Comput.*, vol. 34, no. 5, pp. 351–354, 1996.

Xiayi Liu received the B.Eng. degree from Xi'an University of Technology, Xi'an, China, and the M.Sc. degree from Xi'an University of Technology, China, in 2011 and 2014, respectively. He is currently working toward the Ph.D. degree from the Faculty of Mechanical and Precision Instrument Engineering, Xi'an University of Technology, China.

From 2015 to 2019, he was an Exchange Student with Chiba University, Chiba, Japan. His research interest includes biomicrofluidics, multiphase flow dynamics, and electrical impedance tomography.

Jiafeng Yao received the B.Eng. degree from the First Aviation Academy of PLA, Jilin, China, the M.Sc. degree from Nanjing University of Science & Technology, Nanjing, China, and the Ph.D. degree from Kumamoto University, Kumamoto, Japan, in 2008, 2011, and 2011, respectively.

He is currently a Lecturer with the College of Mechanical & Electrical Engineering, Nanjing University of Aeronautics & Astronautics, Nanjing, China. From 2014 to 2016, he was a Research Fellow of Japan Society for the Promotion of Science (JSPS) with the Department of Mechanical Engineering, Chiba University, Chiba, Japan. His research interest includes biomicrofluidics, multiphase flow dynamics, and electrical impedance tomography.

Tong Zhao received the B.S. and M.S. degrees in mechanical engineering from Xi'an University of Technology, Xi'an, China, in 2003 and 2006, respectively, and the Ph.D. degree in mechanical engineering from Nihon University, Tokyo, Japan, in 2010.

From 2010 to 2011, he was a Research Assistant with the Nihon University, Japan. From 2013 to 2015, he was a Fellow of Japanese society for promotion of Science (JSPS) with Chiba University, Chiba, Japan. He is currently an Associate Professor with the School of Mechanical and Precision Instrument Engineering, Xi'an University of Technology, Xi'an, China. His research interests include measurement and numerical simulation of multiphase flow and corresponding multicomponent heat transfer mechanism.

Dr. Zhao was a recipient of the Prestigious Young Researcher Prize of the Asian Particle Technology Council in 2012.

Hiromichi Obara received the B.Eng., M.Sc., and Ph.D. degrees from Tokyo Metropolitan Institute of Technology, Tokyo, Japan.

He is currently an Associate Professor with the Department of Mechanical Engineering, Tokyo Metropolitan University, Tokyo, Japan. From 1998 to 2005, he was an Assistant Professor with Tokyo Metropolitan Institute of Technology, Tokyo, Japan. From 2001 to 2002, he was a Guest Researcher in the National Institute of Standards and Technology, Gaithersburg, MD, USA. His research interests include fluid engineering, bioengineering, electrokinetics, and organ engineering.

Yahui Cui received the B.Eng., M.Sc., and Ph.D. degrees from Xi'an University of Technology (XUT), Xi'an, China.

He is currently a Professor and the dean of the faculty of Mechanical and Precision Instrument Engineering, XUT, China. His research interests include the new type of mechanical transmission device and theory, the new type of vehicle transmission technology research and vehicle components, the principle, simulation and recovery of ancient mechanism, and the techniques of production modeling and simulation.

Dr. Cui is the Academic Leader of Mechanical Design and Theory, XUT, China, the Executive Director of the National Mechanical Principle Teaching Research, the Managing Director of the Shaanxi Provincial Institute of Mechanical Engineering, and the Senior Member of Chinese Mechanical Engineering Society.

Masahiro Takei received the B.Eng., M.Sc., and Ph.D. degrees from Waseda University, Tokyo, Japan.

He is a Professor and the Vice Dean of the Graduate School of Engineering, Chiba University, Chiba, Japan. He was a Guest Researcher with the University of Leeds, Leeds, U.K., in 2007, awarded by the Royal Society. His research interests include multiphase flow dynamics, visualization and measurement, process tomography and inverse problem, microfluidics, and bioapplication.

Dr. Takei is the President of International Society for Industrial Process Tomography (Headquarter U.K.), the Vice Chair Person, a Board Member of American Society of Mechanical Engineers Japan Section, a Board Member of Visualization Society of Japan, a Councilor of the Society of Powder Technology, Japan, a Board Member of Japanese Society Experimental Mechanics, a Guest Editor of *Measurement Science and Technology* (Institute of Physics), a Guest Editor of *Flow Measurement and Instrumentation* (Elsevier), and an Editorial Board Member of the *Journal of Visualization* (Springer).

西安理工大学检索收录证明

检索工具	SCI-E（科学引文索引-扩展）	版本	网络版
收录作者	刘夏移	查证人	冯会勤
作者单位	机械与精密仪器工程学院	查证日期	2018-12-18

PT J
AU Liu, XY
Yao, JF
Zhao, T
Obara, H
Cui, YH
Takei, M
AF Liu, Xiayi
Yao, Jiafeng
Zhao, Tong
Obara, Hiromichi
Cui, Yahui
Takei, Masahiro
TI Image Reconstruction Under Contact Impedance Effect in Micro Electrical Impedance Tomography Sensors
SO IEEE TRANSACTIONS ON BIOMEDICAL CIRCUITS AND SYSTEMS
LA English
DT Article
DE Contact impedance; electric double layer; micro electrical impedance tomography; multilayered microchannel
ID CAPACITANCE TOMOGRAPHY; CELLS; REGULARIZATION
AB Contact impedance has an important effect on micro electrical impedance tomography (EIT) sensors compared to conventional macro sensors. In the present work, a complex contact impedance effect ratio xi is defined to quantitatively evaluate the effect of the contact impedance on the accuracy of the reconstructed images by micro EIT. Quality of the reconstructed image under various xi is estimated by the phantom simulation to find the optimum algorithm. The generalized vector sampled pattern matching (GVSPM) method reveals the best image quality and the best tolerance to xi. Moreover, the images of yeast cells sedimentary distribution in a multilayered microchannel are reconstructed by the GVSPM method under various mean magnitudes of contact impedance effect ratio |xi|. The result shows that the best image quality that has the smallest voltage error U-E = 0.581 is achieved with measurement frequency f = 1 MHz and mean magnitude |xi| = 26. In addition, the reconstructed images of cells distribution become improper while f < 10 kHz and mean value of |xi| > 2400.
C1 [Liu, Xiayi; Zhao, Tong; Cui, Yahui] Xian Univ Technol, Fac Mech & Precis Instrument Engn, Xian 710048, Shaanxi, Peoples R China.
[Yao, Jiafeng] Nanjing Univ Aeronaut & Astronaut, Coll Mech & Elect Engn, Nanjing 210016, Jiangsu, Peoples R China.
[Obara, Hiromichi] Tokyo Metropolitan Univ, Dept Mech Engn, Tokyo 1920397, Japan.
[Takei, Masahiro] Chiba Univ, Dept Mech Engn, Chiba 2630022, Japan.
RP Yao, JF (reprint author), Nanjing Univ Aeronaut & Astronaut, Coll Mech & Elect Engn, Nanjing 210016, Jiangsu, Peoples R China.
EM liu.xy@chiba-u.jp; jiaf.yao@nuaa.edu.cn; tongzhao@xaut.edu.cn; obara@tmu.ac.jp; cyhxut@xaut.edu.cn; masa2@chiba-u.jp
OI
Yao, Jiafeng 0000-0002-6405-0512
Zhao, Tong 0000-0001-9880-0513
FU Bio Assembler [26106708]; National Natural Science Foundation of China [51706098, 51506175]; Natural Science Foundation of Jiangsu Province [BK20170792]
FX This work was supported in part by Bio Assembler, Grant-in-Aid for Scientific Research on Innovative Areas of Japan, under Grant 26106708, in part by the National Natural Science Foundation of China under Grant 51706098 and Grant 51506175, and in part by the Natural Science Foundation of Jiangsu Province under Grant BK20170792. This paper was recommended by Associate Editor S. Sonkusale. (Corresponding author: Jiafeng Yao.)
NR 23
TC 3
Z9 3
U1 15
U2 15
PU IEEE-INST ELECTRICAL ELECTRONICS ENGINEERS INC
PI PISCATAWAY
PA 445 HOES LANE, PISCATAWAY, NJ 08855-4141 USA
SN 1932-4545
EI 1940-9990
J9 IEEE T BIOMED CIRC S
JI IEEE Trans. Biomed. Circuits Syst.
PD JUN
PY 2018
VL 12
IS 3
SI SI
BP 623
EP 631
DI 10.1109/TBCAS.2018.2816946
PG 9
WC Engineering, Biomedical; Engineering, Electrical & Electronic
SC Engineering
GA GI6FW
UT WOS:000434466000017
PM 29877825
DA 2018-12-18
ER